PCCP

High-temperature thermoelectric transport behavior of Al/γ-Al2O3 interface: Impact of electron and phonon scattering at nanoscale metal-ceramic contacts

Journal:	*Physical Chemistry Chemical Physics*
Manuscript ID	CP-ART-03-2018-001374.R1
Article Type:	Paper
Date Submitted by the Author:	14-Apr-2018
Complete List of Authors:	Samanta, Pabitra; Jackson State University, Department of Chemistry Leszczynski, Jerzy; Jackson State University, Department of Chemistry

High-temperature thermoelectric transport behavior of Al/γ-Al_2O_3 interface: Impact of electron and phonon scattering at nanoscale metal-ceramic contacts

Pabitra Narayan Samanta and Jerzy Leszczynski*

Interdisciplinary Center for Nanotoxicity, Department of Chemistry, Physics and Atmospheric Sciences, Jackson State University, Jackson, MS 39217, USA

Abstract: The thermoelectric transport properties of metal-ceramic interface based on Al and γ-Al_2O_3 are explored by employing the non-equilibrium Green's function formalism (NEGF) coupled with density functional theory (DFT). However, to acquire the phonon thermal conductance, the parameterized ReaxFF potential is utilized for computing the intrinsic force constants of propagating phonons across the interface. Several interfacial electronic properties such as charge transfer, potential barrier, and atomic orbital overlap are critically analyzed based on the DFT derived results of electrostatic difference potential, electron density difference, and the spin-polarized density of states in the fully relaxed structure of the interface. Within the NEGF framework, both the electron and phonon transmission coefficients are estimated for the variations of bias voltage and temperature gradient across the interface. The strong orbital overlapping and the scattering of electrons and phonons at the nanometer-size interface suppress the lattice thermal conductivity significantly compared to the electron transport, which in turn enhances the thermoelectric performance of the Al/Al_2O_3 composite, in contrast to the bulk material of Al. Moreover, a steep rise of power factor induced by increased transmission of charge carriers with temperature improves the energy conversion efficiency of the material. The present findings could pave the way for developing thermoelectric materials based on metal-ceramic composite.

Keywords: Al/γ-Al_2O_3 interface, DFT-NEGF approach, electron and phonon transmission, thermoelectric performance

*E-mail: jerzy@icnanotox.org

1. Introduction

The exploration of multilayered metal-ceramic interfaces as the potential candidates in modern nano-transistors and electronic devices has stimulated great interest and intensive research on the electro-thermal transport properties of Al/Al_2O_3 interfaces [1-3]. For efficient thermal management and to alleviate the self-heating effects in microelectronic devices, the quest for advanced materials exhibiting higher electrical and thermal conductivities has gained attention of the researchers. Owing to the unique electronic properties of Al/Al_2O_3 interfaces such as higher mechanical strength, better electro-statics, high thermal conductivity and corrosion resistance, much effort has been paid to employ the Al/Al_2O_3 composite as a promising material in a range of technological applications starting from catalysis, sensors, corrosion protection, and thermal barriers to microelectronics, single-electron transistors, and energy storage [4-10].

The advent of Al/Al_2O_3 interface has spurred to investigate the electronic structure and properties of this metal-ceramic composite. By employing both the local density approximation (LDA) and the generalized gradient approximation (GGA) based exchange-correlation functional, Siegel et al. [11] carried out quantum mechanical computations to predict the structure and adhesion properties of both the O-terminated and Al-terminated Al (111)/α-Al_2O_3 (0001) interface. Streitz and Mintmire [12, 13] explored the applicability of molecular dynamics (MD) simulation to estimate the surface energies as well as determine the elastic properties of the Al/α-Al_2O_3 interface by implementing interatomic empirical potential associated with variable charge transfer between cations and anions. In order to evaluate the critical temperature of nonwetting-wetting transition and investigate the structural, energetic, and adhesion properties of Al/Al_2O_3 interface, Zhang et al. [14] conducted MD simulation study within the framework of reactive force field (ReaxFF) approach. Later, a detailed theoretical study has been carried out by Pilania et al. [15] with the recognition of macroscopic mechanical behavior of the coherent and semi-coherent Al/α-Al_2O_3 interfaces. In that study, they performed an anneal-and-quench MD calculation by invoking a mixed metallic-ionic atomistic model derived from modified embedded atom method (MEAM) potential and the charge transfer ionic potential (CTIP) model.

With the advancement of nanotechnology the synthesis and fabrication of multilayered metal-ceramic nano-composites portraying significant enhancement in the mechanical strength become feasible to be realized experimentally [16-19]. Goswami et al. [20] demonstrated the impact of annealing technique to the escalation of mechanical strength of the sputter deposited Al/γ-Al_2O_3 multilayered

composite having interlayer spacing of about 100 nm. The rise in hardness was found to be associated with the precipitation of ultra-fine γ-Al_2O_3 in the Al layers. Furthermore, the formation of Al/Al_2O_3 interface is assessed by performing density functional theory (DFT) based calculations using Perdew-Burke-Ernzerhof (PBE) exchange correlation functional and projector-augmented wave (PAW) based pseudopotential. The predicted lower decohesion energy for the interaction between (001) surfaces of Al and γ-Al_2O_3 affirms the stability of the composite as well as the formation of strong bonding across the interface. By exploiting atomic layer deposition and magnetron sputter deposition techniques, Costescu et al. [21] fabricated the metal-ceramic interface of dissimilar materials of W/Al_2O_3 which is indicated to be advantageous in attaining ultra-low thermal conductivity. Muliana and co-workers [22] studied the thermo-mechanical properties of Al-Al_2O_3 composites prepared by using powder metallurgy method; and evaluated those parameters that control the elastic and thermal characteristics of composites.

Albeit a number of theoretical as well as experimental research works have been devoted to determine the structural and mechanical properties of Al/Al_2O_3 interfaces, the electron and thermal transport properties of the aluminum-alumina composite have not been widely studied. In order to check the influence of interface geometry and the corresponding barrier heights and widths on the electron tunneling in Al/Al_2O_3/Al junctions, Koberidze et al. [23] measured the differential conductance as a function of applied bias voltage, and compared the results with those obtained from DFT based calculations within the Wentzel-Kramers-Brillouin (WKB) approximation. The electron transport through the Al/Al_2O_3 tunnel barrier is predicted to be explicitly dependent on the atomic disposition and the stoichiometry at the Al/Al_2O_3 interface. Apart from that, efforts are being paid to explore the fundamental mechanism of thermal transport across the metal-ceramic interface. Hopkins et al. [24] estimated the thermal boundary conductance for the Al/Al_2O_3 interface at different temperatures from 300K to 500K applying the transient thermoreflectance (TTR) technique. The measurements anticipate an anomalously high thermal boundary conductance at an elevated temperature, which exceeds the probable maximum thermal conductance emanating from harmonic phonon transmission across the interface. The experimental results are further compared with the theoretically computed values derived from models dealing with phonon scattering such as diffuse mismatch model (DMM) and phonon radiation limit (PRL). However, the proposed theoretical models could not satisfactorily explain the anomalous high interface conductance due to the exclusion of inelastic phonon scattering at the

interface. Very recently, the performance of thermoelectric energy generator based on Al_2O_3/ZnO superlattice thin films has been assessed by Park et al. [25].

By performing *ab initio* based calculations, Ching et al. [26] predicted that the γ-Al_2O_3 exhibits a much larger thermal-expansion coefficient compared to α-Al_2O_3. The detailed comparative studies of electronic properties of these two phases of alumina anticipate the existence of high degree of disorder as well as enhanced anharmonicity in γ-Al_2O_3 structure. In addition, compared with α-Al_2O_3, the γ-Al_2O_3 possesses a reduced band gap, which can provide a well balance between the electrical conductivity and Seebeck coefficient. The differences in elastic properties and densities of vibrational states between the metal and ceramic materials generally impede the conveyance of vibrational states across the interface, leading to a suppression of thermal conductivity, and thereby offering another degree of freedom to optimize thermoelectric conversion performance. On the other hand, by using transmission electron microscopy (TEM) and high-resolution electron microscopy (HREM), Yang et al. [27] identified promising thermal stability of Al/Al_2O_3 composite. The exceptionally high thermal resistance of the composite, even above the melting point of Al, emanates from the wetting of the Al_2O_3 network with liquid Al. The supremacy of multilayered Al/γ-Al_2O_3 nanocomposite [20] compared to their pristine bulk counterparts thus motivates us to investigate the thermoelectric properties of metal-ceramic interface composed of Al and γ-Al_2O_3. Albeit a number of literature works addressing the mechanical and thermal stability of Al/Al_2O_3 interface have remained quite accessible, the thermoelectric performance of this composite is seldom studied. The present study explores the thermoelectric conversion efficiency of a microelectronic device of Al/γ-Al_2O_3 interface by performing first-principles based calculations using DFT coupled with non-equilibrium Green's function (NEGF) formalism. The heat transport mechanism is critically analyzed by computing electrical conductance, Seebeck coefficient, as well as electronic and phonon contribution to the thermal conductance at several temperatures. In order to further investigate the electronic transport properties of the Al/ γ-Al_2O_3 composite, the current-voltage (I-V) characteristics have been examined by evaluating the electrical current with the variation in the voltage gradient across the interface.

2. Computational Details

To calculate the quantum transport properties of the Al/Al_2O_3 interface within the NEGF framework, we have adopted a two-probe model consisting of a finite central scattering region (C)

which is connected to two semi-infinite periodic leads (L/R) as the electron or heat baths. Figure 1 displays the proposed atomistic model of the microelectronic device. The central region includes an eight-layered metallic Al surface and a cubic cell of the oxide material (γ-Al_2O_3) with a thickness of about 0.81 nm, which could be sufficient for screening the effect of any surface related phenomenon [15, 20, 25, 28]. A large enough dimension of the central region with a length of about 3.2 nm has been considered to accommodate both the voltage and temperature drop within itself. Apart from that, several attempts have been made to obtain decent interface geometry where both strain mismatch and cell-size are optimum. Prior to the calculations of carrier transport, all the model structures of bulk surface and interface cells are optimized by employing PBE [29] exchange correlation functional with a double zeta polarized (DZP) basis set for both Al and O atoms, and a mesh cut-off energy of 150 Ry. All atomic positions are relaxed until the maximum atomic forces become smaller than 0.05 eV/Å.

As evident from previous experimental and theoretical studies [30-37], the γ-Al_2O_3 has a cubic *fcc*-like defected spinel structure, and the defective nature mainly arise from the presence of Al cation vacancies that are distributed between octahedral and tetrahedral sites in the lattice. However, the presence of octahedral holes is found to be energetically more favorable than tetrahedral holes. In the present work, the models where the vacancies are located at the octahedral sites are considered. Herein, we chose the (100) surface of γ-Al_2O_3, as the (100) and (110) surfaces are predicted to be dominant in γ-Al_2O_3 [33]. Further, the efficiency and robustness of the model structure of (100) surface of γ-Al_2O_3 are verified by comparing the estimated lattice parameter and band gap values with those of earlier studies. The lattice constant for the proposed supercell model of γ-Al_2O_3 is computed to be 7.99 Å, which corroborates well with the experimentally determined value of 7.90 Å [38]. The calculated band gap for γ-Al_2O_3 is about 4.25 eV, which corroborates well with the previous result reported by Ching et al. [26]. The DFT derived direct band gap is underestimated by about 4.0 eV compared to the experimental result, and this is in well agreement with the previous theoretical predictions using DFT [39-41]. The fully relaxed structures of Al and γ-Al_2O_3 are then utilized to construct the interface geometry by considering all possible stacking orientations between these two materials. In order to make the surface cells commensurate, we employ the lattice matching method [42] that seeks the plausible candidates by considering convenient effects on the lattice constant in the direction perpendicular to the interface plane i.e. the Poisson effect. The implemented method thus facilitates the identification of epitaxial interface where both the strain and the area of the coincidence interface cell are minimized. During the interface simulation, the DFT derived in-plane lattice constant of bulk Al, which is within 1% of the γ-

Al_2O_3 lattice constant, is used. The resultant interface is comprised of Al_2O_3 supercell with lattice parameter (a = 0.76 nm, b = 0.81 nm, c = 1.6 nm), and Al supercell with lattice parameter (a = 0.77 nm, b = 0.81 nm, c = 1.6 nm). The predicted low-strain epitaxial interface, with a mean strain of 0.2%, is further subjected to relaxation by DFT based method. The interface geometries are optimized by employing LBFGS (Limited-memory Broyden Fletcher Goldfarb Shanno) algorithm. The k-points in the Monkhorst-Pack grid are set to (4 x 4 x 4) and (4 x 4 x 1) for the relaxation of single-phase supercells and interface cells, respectively. Moreover, during the structural relaxation a vacuum spacing of 20 Å is added along the "C" direction of the supercell to overcome the spurious interactions caused by periodic boundary condition. The Poisson equation is solved using a Fast Fourier Transform (FFT) solver. Further, to solve the Poisson equation, we assign periodic boundary conditions in A-B directions, and Dirichlet boundary condition in the transport direction (i.e. the C-direction). The lowest energy structure of the Al/Al_2O_3 interface shows a strong resemblance to that obtained by Goswami et al. [20].

In order to calculate the linear transport properties of the two-probe model using DFT-NEGF method as implemented in QuantumWise ATK software package [43], the electron transport is assumed to travel ballistically. Further, the quantum transport properties of this nano-structured device is computed by employing LDA based exchange-correlation potential, and single-zeta plus polarization (SZP) basis sets. The Brillouin zone of the whole structure is sampled with (1 x 1 x 100) Monkhorst-Pack k-mesh in the transport direction. Within the NEGF formalism [44, 45], the electron transmission coefficient which determines the probability of electrons transferring between the two semi-infinite leads can be evaluated by

$$T_e(E) = Tr[\Gamma_L(E)G^r(E)\Gamma_R(E)G^a(E)] \quad (1)$$

where $G^r(E)$ represents the retarded Green's function; $G^a(E) = \left(G^r(E)\right)^\dagger$ is the advanced Green's function; and $\Gamma_{L/R}$ signify the coupling interaction with left/right lead. The retarded Green's function is calculated as

$$G^r(E) = [EI - H_C - \sum_L^r - \sum_R^r]^{-1} \quad (2)$$

where H_C is the Hamiltonian of the central region containing the interface, and I is the identity matrix. $\sum_L^r$ and $\sum_R^r$ denote the self-energy matrices for the left and right semi-infinite leads.

Now, exploiting Landauer-Büttiker formalism [46, 47], the electrical current can be computed as

$$I = \frac{2q}{h} \int_{-\infty}^{+\infty} T_e(E)\,[f(E,\mu_L) - f(E,\mu_R)]\,dE \quad (3)$$

where factor 2 counts for spin degeneracy; h is the Planck's constant; q is the electrical charge of carrier; $f(E,\mu)$ is the Fermi distribution function; $\mu_{L,R}$ are chemical potentials of the left and right leads; and T_e indicates the transmission function per spin (considering up / down) derived from self-consistent DFT-NEGF calculations. Apart from that, the applied bias voltage (V_b) between the two leads is related to the chemical potential as, $(\mu_L - \mu_R) = V_b \times q$.

Deploying the concept of linear coherent transport, in the near equilibrium region, the physical quantities related to the thermoelectric properties of the device viz. electrical conductance (G_e), Seebeck coefficient (S), and electrical thermal conductance (K_e) can be obtained as [45, 47]

$$G_e = q^2 \times L_0 \tag{4}$$

$$S = \frac{1}{qT} \times \frac{L_1}{L_0} \tag{5}$$

and

$$K_e = \frac{1}{T} \times \left(L_2 - \frac{L_1^2}{L_0}\right) \tag{6}$$

Where L_n is expressed as

$$L_n = \frac{2}{h} \int_{-\infty}^{+\infty} T_e(E) \left(-\frac{\partial f(E,\mu)}{\partial E}\right) (E - \mu)^n \, dE \tag{7}$$

The procedure for computing the phonon transmission using NEGF technique is the same as the electrical transport after two substitutions [44]

$$EI \rightarrow \omega^2 M_a$$

and

$$H_C \rightarrow K_C$$

where ω is the frequency; M_a denotes the diagonal matrix having the elements describing the masses of atoms; and K_C represents the dynamical matrix of the central region. Similarly, the self-energy matrices of the two semi-infinite leads, and hence the retarded Green's function are also computed as a function of ω. After that, the phonon thermal conductance can be evaluated by exploiting Landauer formalism [45, 48]

$$K_{Ph}(T) = \frac{1}{2\pi} \int_0^{\infty} \hbar\omega \, T_{Ph}(\omega) \times \left(\frac{\partial B(\omega,T)}{\partial T}\right) d\omega \tag{8}$$

where $B(\omega,T)[= \left(e^{\hbar\omega/k_BT} - 1\right)^{-1}]$ is the Bose-Einstein distribution at average temperature T; and k_B is the Boltzmann constant. $T_{Ph}(\omega)$ describes the phonon transmission coefficient.

Now, in the linear transport regime, the temperature difference between the two leads is very small, i.e. $\Delta T = T_L - T_R \approx 0$; and thus we can replace the $\left(\frac{\partial B(\omega,T)}{\partial T}\right)$ with $\frac{\hbar\omega}{k_B T^2} \times \frac{e^{\hbar\omega/k_B T}}{\left(e^{\hbar\omega/k_B T}-1\right)^2}$. Upon substitution, the above equation can be expressed as [44]

$$K_{Ph}(T) = \frac{\hbar^2}{2\pi k_B T^2} \int_0^\infty \omega^2 \, T_{Ph}(\omega) \times \frac{e^{\hbar\omega/k_B T}}{\left(e^{\hbar\omega/k_B T}-1\right)^2} \, d\omega \quad (9)$$

It is noteworthy to mention that, the phonon thermal conductance calculations are carried out in the absence of anharmonic phonon-phonon interaction. Moreover, the phonon transmission coefficient is computed based on parameterization of ReaxFF potential [49, 50] for Al and O as implemented in ATK QuantumWise package.

Finally, the thermoelectric figure of merit of the microelectronic device is estimated by using the following expression:

$$ZT = \frac{G_e \, S^2 \, T}{(K_e + K_{Ph})} \quad (10)$$

3. Results and Discussions

In order to comprehend the impact of surface interactions between γ-Al_2O_3 and Al on the quantum transport behavior of the microelectronic device, the electrostatic difference potential (EDP) and electron difference density (EDD) are evaluated for the Al/Al_2O_3 interface material. EDP refers to the difference between the electrostatic potential of the self-consistent valence electron density and the electrostatic potential derived from a superposition of atomic valence electronic densities. The EDP value (ΔV_E) is estimated by solving the Poisson equation where the charge density is extracted from the electron difference density. The computed average EDP along the C axis of the device (as defined in Figure 1) as well as the cut plane surface of EDP is depicted in Figures 2(a) and 2(b), respectively. The higher the value of ΔV_E, the more difficult it is for charge carriers to cross the barrier. Figure 2(a) reveals that there is a very small protrusion of the potential barrier for charge carriers at the Al/Al_2O_3 contact region as indicated by black arrow. This leads to the conclusion of strong covalent interaction between the two surfaces. Further, the oscillations of EDP are relatively small in the metallic Al regions near the electrodes, reflecting the self-consistent charge distribution is not considerably different from the atomic valence charges in those regions. The surface map portrayed in Figure 2(b) manifests that the ΔV_E is more positive around the site of interface, triggering a higher difference density or charge

accumulation near the interface. To illustrate the charge re-distribution, we also emphasize on the analysis of EDD obtained from difference between the self-consistent valence charge density and the superposition of the atomic valence charge densities. A negative value of EDD signifies charge depletion, while any positive value is indicative of charge accumulation. The small changes in EDD as rendered in Figure 2(c) imply a prominent charge transfer across the interface, and there by suggesting strong interaction between the two surfaces. Since the robust interaction between γ-Al_2O_3 and Al materials furnishes enough electron density, which when subtracted from the initial or neutral electron density leads to the lowering of EDD. To assess the binding strength quantitatively at the metal-ceramic interface, the interface energy is calculated in the optimized structure of interface at the PBE/DZP level of theory. The DFT derived energies of fully relaxed geometries of Al/Al_2O_3 composite and the individual Al and γ-Al_2O_3 materials are used to compute the interface energy:

$$E_{interface} = \frac{E^{SC}_{Al/Al_2O_3} - E^{S}_{Al} - E^{S}_{Al_2O_3}}{2}$$

where E^{SC}_{Al/Al_2O_3} refers to the electronic energy of the supercell of Al/Al_2O_3 interface after relaxation. E^{S}_{Al} is calculated by optimizing the Al surface after eliminating all atoms associated with Al_2O_3 in the supercell, and $E^{S}_{Al_2O_3}$ is computed after removing all atoms corresponding to Al. The appearance of factor of two in the denominator of the above expression accounts for the presence of two surfaces within a supercell. A negative value of $E_{interface}$ is indicative of favorable interaction between the two surfaces. For the lowest energy structure of Al/Al_2O_3 interface cell, the area normalized interfacial energy is estimated to be -5.4 eV/Å^2.

To gain insight into the electronic properties of the edge contacts formed between Al_2O_3 and Al surfaces, we further examine the energy-position resolved local density of states (LDOS) of the device. Figure 3 illustrates the LDOS map along with electron transmission in the energy range [-10, 10] eV relative to the Fermi energy of the interface. In the LDOS diagram, the Z-distances correspond to the channel regions of the two-probe device. The dark and colored bright regions in the LDOS map unveil the absence and presence of the electronic states, respectively. The states of metal-semiconductor interface are precisely portrayed in Figure 3, and the interface is identified to be located around 15 Å. A closer look at the vicinity of the Fermi level indicate that the right side of the device consisting of the Al layers is metallic in nature, and the computed band gap of γ-Al_2O_3 is reproduced on the left side. There are significant changes in the local densities of electronic states of Al atoms near the interface as compared to those in depth. When the metal and the oxide material come in electrical contact, the two

Fermi levels are forced to coincide, and electrons transfer from the oxide into the metal site. This leads to the onset of an excess of negative charge on the metal surface and a negative charge depletion zone in the Al_2O_3 near its surface. The excess charges create an interface dipole followed by an electric field directed from the oxide to the metal. This electric field now corresponds to a gradient of the electrical potential in the depletion layer. As revealed by the projected transmission spectra, the presence of interface of two dissimilar materials gives rise to the formation of a potential barrier which in turn may suppress the electron transport. To study the conductance behavior of the two-probe model of multilayered Al/Al_2O_3 interface, we also conduct the projected device density of states (PDDOS) analyses. The PDDOS spectra estimated from spin polarization calculations at the interface region as well as close to the Al_2O_3 electrode are delineated in Figures 4(a) and 4(b), respectively. However, it can be seen that the overall patterns of up and down DOS-components do not alter significantly, and effectively remain the same for both cases. The comparison of PDDOS spectra clearly unveils that, due to a strong coupling of outermost orbitals at the interface the band gap nature of γ-Al_2O_3 closer to the Fermi level is completely diminished, and it acquires a mixed metal-semiconductor character. This is in well agreement with the results obtained from the projected LDOS analysis. Moreover, it is important to notice that the electronic structure adjacent to the Fermi level is mainly governed by the Al p-orbitlas.

In addition to the aforementioned investigations, we appraise the transmission spectrum that characterizes the electrical behavior of the proposed two-probe device. As mentioned in the previous section, electrical parameters such as conductance, thermal conductance, and Seebeck coefficient contributing to the thermoelectric figure of merit can be uniquely determined from the transmission coefficient. The computed transmission coefficients are plotted in Figure 5 as a function of energy, when no bias voltage is applied. The Fermi level has been set to $E_F = 0$ for simplicity. Transmission spectrum demonstrates that the onset of electron transmission states takes place at about 5.9 eV. For the energy value of 5.9 eV, the transmission coefficient is calculated as ~0.33. Further, the forbidden region for electron transport with respect to the Fermi energy level is consistent with the band gap of γ-Al_2O_3. This band-gap characteristic is retained with increasing bias voltage, as substantiated by computed transmission spectra at several bias voltages varied from -1.0V to +1.0V. However, the interface-induced scattering appears to be more significant with the increase in applied bias voltage.

In order to explore the phonon thermal conductance properties of the metal-ceramic interface, we subsequently delve into a quantitative analysis of phonon transmission by exploiting the dynamical

matrix method within the NEGF framework. Since the size of the proposed Al/Al_2O_3 composite is much shorter than the mean free path of electrons in Al and Al_2O_3 systems [51, 52], the transport mechanism turns out to be ballistic rather than diffusive in nature. In such cases, NEGF method coupled with first-principles calculations can be utilized to explore the thermoelectric properties in the ballistic regime. However, the usage of DFT based methods for the phonon transport simulation of a two-probe model as illustrated in Figure 1 with a length of 3.2 nm and width of about 0.81 nm entails enormous computational resources. To mitigate this constraint we employ classical force field based method. Molecular dynamics (MD) based methods [53, 54] have been widely used to study the phonon thermal conduction. It does not rely on any thermodynamic-limit assumption, and thus this MD method is readily applicable to study the ballistic thermal conductance in nanoscale systems. Previously, the DFT-NEGF approach followed by estimations of force constants of propagating phonons using MD has been proved to be a reliable method to explore the electrical and thermal transport properties of Al-Si based metal-semiconductor interface [55]. Moreover, the parameterized ReaxFF potential has been successfully deployed by Zhang et al. [14] to determine the structural, mechanical, and adsorption properties of Al/Al_2O_3 interfaces, and proved to be a reliable method in measuring the critical temperature of nonwetting-wetting transition. Figure 6 portrays the computed phonon thermal conductance (K_{Ph}) for the Al/γ-Al_2O_3 interface as a function of temperature. At room temperature, the predicted intrinsic phonon thermal conductance in the quasi ballistic transport regime is about 0.08 nW/K. However, at the higher temperatures (> 500 K), K_{Ph} is found to be constant over a wide range of temperatures, and it reaches a value of 0.09 nW/K.

To examine the effect of Fermi level shift with temperature on the thermoelectric conversion efficiency of the device, the ZT values are computed using equation (10) at several temperatures, and compared. Figure 7(a) unveils the characteristics of ZT curves as a function of Fermi level position at different temperatures. The characteristic double-peak structure of the ZT curve emanates from the line shape of the Seebeck coefficient (Figure 7(b)). The asymmetry in ZT curve is attributed to the contribution of valence and conduction bands at a given temperature, since ZT is a function of both temperature and Fermi energy. The two main peaks in ZT correspond to valence band maximum (VBM) and conduction band minimum (CBM), which are indicated by vertical dashed lines in Figure 7(a). As ZT is directly proportional to temperature according to equation (10), the amplitude of ZT generally enhances with the rise in temperature. Moreover, the enhancement of temperature broadens the Fermi distribution, which in turn tends to populate the electronic states in energies higher than the Fermi

level. These newly occupied states now contribute to both electrical and thermal conduction, and thereby improve the thermoelectric performance of the device. A closer inspection of the ZT curves indicate that the ZT value reaches maximum at a given temperature only when the Fermi level moves into conduction band compared to when it moves into valence band. Next, we report the variations of Seebeck coefficients at different temperatures with respect to the Fermi level position. Figure 7(b) portrays the predicted antisymmetric characteristics of the temperature dependence of the Seebeck coefficient. This is because the sub-band is symmetric and the transmission function is an even function in equation (7), but L_1 is an odd function about $(E - \mu)$. Further, the peak at an elevated temperature is suppressed more compared to that obtained at 300 K. At higher temperature, the Fermi-Dirac distribution function $f(E, \mu)$ is smoother at the Fermi surface, leading to the smaller value of $(\partial f / \partial E)$ in equation (7) for L_1. As a consequence, the S value estimated from equation (5) decreases with the increase of temperature.

To improve the thermoelectric conversion efficiency of the device, a detailed investigation of temperature dependence of thermoelectric parameters of the Al/γ-Al_2O_3 interface has been performed quantitatively. The alterations of electrical conductance and Seebeck coefficient with the rise of temperature are distinctly shown in Figures 8(a) and 8(b), respectively; while Figure 8(c) describes the temperature dependence of the power factor $(G_e S^2)$ of the device. Owing to the enhancement of electron transport in the conduction band the electrical conductivity increases with increasing temperature. The temperature dependence of Seebeck coefficient is diametrically opposed to the characteristics of electronic conductance. Due to the usual interdependence of transport parameters, the augmentation of electronic conductance tends to suppress the Seebeck coefficient with the rise in temperature. Nonetheless, looking into the plot of S as a function of T, it can be observed that the magnitude of S increases up to 300 K, and then decreases with increasing temperature till 900 K. The suppression of S values is strongly correlated with the thermal excitation process of electrons across the band gap as well as the mobility of charge carriers. Since the holes carry the opposite charge from electrons, the conduction of holes having higher mobility and smaller effective mass than the electron carriers significantly reduces the S value. Further, the peak around 300 K in the curve of $S(T)$ is attributed to the maximum point of the electron-transmission-weighted average value of $(E - \mu)$ in equation (7) for L_1. Next, we report the power factor of the device that quantifies the potentiality of a material to produce the electrical power. As delineated in panel 8(c), the estimated power factor which

depends on two contrasting terms G_e and S^2 is found to monotonically increase beyond the temperature 500 K.

To analyze the effect of temperature on ZT, we also calculate the thermal conductance (K) of the device which is composed of electronic thermal conductance (K_e) and phonon thermal conductance (K_{Ph}). In Figure 8(d), we report the variations of K_e and K_{Ph} as a function of temperature (T). Because the charge carriers are being the heat carriers, the K_e value is found to gradually increase with the increase of T. However, the estimated K_{Ph} values attain a constant value corresponding to the classical limit when T > 400 K. As the phonon thermal conductance calculations are performed within the framework of ballistic transport, the non-linear effect of phonon-phonon scattering which reduces the transmission coefficients at high temperature is absent in the present computational study. Albeit the previous investigations of electronic structure and interband transitions of α-Al_2O_3 using temperature-dependent vacuum ultraviolet spectroscopy reveal that the electronic structure is linear upto 1700 K, which emanates from the linear characteristic of the thermal lattice expansion and the vibrational Debye-Waller factors [56]. Therefore, the total thermal conductance is driven by the competition between electrical and phonon conductances. Figure 8(e) delineates the characteristics of temperature dependence of total thermal conductance $(K_e + K_{Ph})$ of the device. At low temperature the phonons play the crucial role in thermal transport, whereas the electrons perform the leading role in thermal transport at higher temperature. The thermoelectric performance of the Al/γ-Al_2O_3 interface under the influence of temperature is attributed to the combined impact of all four quantities entering the figure of merit expression. Figure 8(f) illustrates the integrated impacts from all of the four quantities. The results clearly manifest that ZT increases monotonically with temperature. Thus, for the Al/γ-Al_2O_3 interface, the temperature dependence of the magnitude of ZT is predicted to be strong and the estimated ZT vales vary between 0.03 – 0.62 in the whole temperature range from 100 K to 1000 K. At room temperature (T = 300 K), the estimated ZT value reaches at 0.1 for the Al/γ-Al_2O_3 interface, while ZT is much smaller than 0.1 for the bulk material of Al [55]. It is noteworthy to mention that, the predicted ZT of this metal-ceramic interface at T = 300 K is much higher than the previously reported value of 0.014 for the Al_2O_3/ZnO superlattice films having the same thickness of Al_2O_3 layers (about 0.82 nm) [25].

To gain insight into the electronic transport properties of the two-probe model, we additionally report the current-voltage (I-V) characteristics of the metal-ceramic interface under non-equilibrium conditions employing Landauer-Büttiker formalism. Figure 9 portrays the computed steady-state

electrical current through the Al/γ-Al_2O_3 interface at different bias voltages. The applied bias voltage (V_b) has been varied from -1.0 to +1.0 V. The current-flow from left to the right electrode refers to the positive bias, while that from right to the left corresponds to the negative bias. As anticipated, the I-V curves are asymmetric in nature in the positive and negative external bias voltages. This anomaly can be explained from the comparison of projected LDOS analyses at forward and reverse bias voltages. Figures 10(a) and (b) depict the computed LDOS map at +0.7 V and – 0.7 V, respectively. In case of forward bias condition, the chemical potential of the right lead (ϵ_R) is elevated compared to that of left lead (ϵ_L), and thereby the net flow of electrons takes place from the right to the left lead, and the current transmits in the opposite direction. However, the propagation of electrons is restricted by the presence of a potential barrier induced by the depletion region across the interface, fostering the suppression of current flow through the interface. Such type of potential barrier is absent within the bias window at – 0.7 V, as reflected by calculated LDOS map as well as projected transmission spectra under reverse bias condition.

4. Conclusion

First-principle quantum transport calculations based on combined methods of DFT and NEGF are performed to study the electro-thermal transport properties of Al/γ-Al_2O_3 interface. We carried out detailed investigation of electronic properties of this metal-ceramic interface by employing the Kohn-Sham density functional theory. The characteristics of interface charge transfer, potential barrier, and atomic orbital overlap are determined from the analyses of electrostatic difference potential, electron density difference, and density of states in the optimized interface geometry. The obtained results unveil the strong interaction between the surfaces of two dissimilar materials. The stability of metal-ceramic interface is substantiated by computed area normalized interface energy which is predicted to be -5.4 eV/$Å^2$ at the PBE/DZP level of theory. After that, the electron transport mechanism through the two-probe model of Al/Al_2O_3 interface has been explored in the ballistic transport regime by using the NEGF approach. Later with the help of parameterized ReaxFF potential, the phonon transmission coefficients are computed at several temperatures. The thermal conductance due to lattice vibration is estimated to be 0.08 nW/K at 300 K.

Next, to assess the energy conversion efficiency of the Al/γ-Al_2O_3 composite, the magnitude of thermoelectric figure of merit is evaluated with the variation of temperature gradient across the

interface. The ZT value of proposed thermoelectric material based on metal-semiconductor interface reaches about 0.1 at 300 K, and maximizes to 0.6 when the temperature approaches to 1000 K. The augmentation of ZT with the enhancement of temperature emanates from the gradual increase of power factor of the device as well as the suppression of lattice thermal conductivity compared to the electronic conductance due to the scattering of phonons and electrons at the interface. Finally, the current-voltage characteristics of the microelectronic device composed of Al/γ-Al_2O_3 interface have been reported. The results clearly manifest that the magnitude of measured electrical current increases with the rise of applied bias voltage. However, the current production shows significant improvement only when the bias is applied to the metallic Al electrodes. The present findings could be helpful in guiding the design and fabrication of Al-Al_2O_3 composite for enhancing the thermoelectric conversion efficiency of microelectronic devices.

Acknowledgments

The financial assistance provided by the Office of Naval Research (ONR), USA through the Grant N00014171306 is gratefully acknowledged.

References

1. M. W. Finnis, *J. Phys: Cond. Mat.*, 1996, **8**, 5811-5836.
2. P. E. Hopkins, R. N. Salaway, R. J. Stevens and P. M. Norris, *Int. J. Thermophys.*, 2007, **28**, 947-957.
3. M. Koberidze, A. V. Feshchenko, M. J. Puska, R. M. Nieminen and J. P. Pekola, *J. Phys. D: Appl. Phys.*, 2016, **49**, 165303.
4. M. Ksiazek, N. Sobczak, B. Mikulowski, W. Radziwill and I. Surowiak, *Mater. Sci. Eng. A*, 2002, **324**, 162-167.
5. Q. Fu and T. Wagner, *Surf. Sci. Rep.*, 2007, **62**, 431-498.
6. M. Watanabe, *Phys. Rev. B*, 2004, **69**, 094509.
7. T. A. Palomaki, S. K. Dutta, H. Paik, H. Xu, J. Matthews, R. M. Lewis, R. C. Ramos, K. Mitra, P. R. Johnson, F. W. Strauch, A. J. Dragt, C. J. Lobb, J. R. Anderson and F. C. Wellstood, *Phys. Rev. B*, 2006, **73**, 014520.
8. D. D. Shen, R. Zhu, W. W. Xu, J. J. Chang, Z. M. Ji, G. Z. Sun, C. H. Cao and J. Chen, *Chin. Sci. Bull.*, 2012, **57**, 409-412.
9. F. Behzadi, M. Moradi, H. R. Karimi and A. Gharavi, *Vacuum*, 2014, **99**, 204-210.
10. T. D. Dao, K. Chen, S. Ishii, A. Ohi, T. Nabatame, M. Kitajima and T. Nagao, *ACS Photonics*, 2015, **2**, 964-970.
11. D. J. Siegel, L. G. Hector Jr. and J. B. Adams, *Phys. Rev. B*, 2002, **65**, 085415.
12. F. H. Streitz and J. W. Mintmire, *Compos. Interfaces*, 1994, **2**, 473-484.
13. F. H. Streitz and J. W. Mintmire, *Phys. Rev. B*, 1994, **50**, 11996-12003.
14. Q. Zhang, T. Çağın, A. v. Duin, W. A. Goddard III, Y. Qi and L. G. Hector Jr., *Phys. Rev. B*, 2004, **69**, 045423.
15. G. Pilania, B. J. Thijsse, R. G. Hoagland, I. Lazić, S. M. Valone and X.-Y. Liu, *Sci. Rep.*, 2014, **4**, 4485.
16. A. T. Alpas, J. D. Embury, D. A. Hardwick and R. W. Springer, *J. Mater. Sci.*, 1990, **25**, 1603-1609.
17. G. T. Mearini and R. W. Hoffman, *J. Electron. Mater.*, 1993, **22**, 623-629.
18. D. O. Northwood and A. T. Alpas, *Nanostruct. Mater.*, 1998, **10**, 777-793.
19. X. Deng, N. Chawla, K. K. Chawla, M. Koopman and J. P. Chu, *Adv. Eng. Mater.*, 2005, **7**, 1099-1108.
20. R. Goswami, C. S. Pande, N. Bernstein, M. D. Johannes, C. Baker and G. Villalobos, *Acta Mater.*, 2015, **95**, 378-385.
21. R. M. Costescu, D. G. Cahill, F. H. Fabreguette, Z. A. Sechrist and S. M. George, *Science*, 2004, **303**, 989-990.
22. P. Gudlur, A. Muliana and M. Radovic, *Composites: Part B*, 2014, **58**, 534–543.

23. M. Koberidze, A. V. Feshchenko, M. J. Puska, R. M. Nieminen and J. P. Pekola, *J. Phys. D: Appl. Phys.*, 2016, **49**, 165303.
24. P. E. Hopkins, R. N. Salaway, R. J. Stevens and P. M. Norris, *Int. J. Thermophys.*, 2007, **28**, 947-957.
25. N.-W. Park, J.-Y. Ahn, T.-H. Park, J.-H. Lee, W.-Y. Lee, K. Cho, Y.-G. Yoon, C.-J. Choi, J.-S. Park and S.-K. Lee, *Nanoscale*, 2017, **9**, 7027-7036.
26. W. Y. Ching, L. Ouyang, P. Rulis and H. Yao, *Phys. Rev. B*, 2008, **78**, 014106.
27. Z. Yang, L. He, J. Chen, H. Cong and H. Ye, *J. Mater. Res.*, 2003, **18**, 272-278.
28. P.W.M. Jacobs, Y.F. Zhukovskii, Y. Mastrikov, Y. N. Shunin, *Comput. Model. New Technol.*, 2002, **6**, 7–28.
29. J. P. Perdew, K. Burke and M. Ernzerhof, *Phys. Rev. Lett.*, 1996, **77**, 3865.
30. X. Krokidis, P. Raybaud, A. E. Gobichon, B. Rebours, P. Euzen and H. Toulhoat, *J. Phys. Chem. B*, 2001, **105**, 5121-5130.
31. M. Digne, P. Sautet, P. Raybaud, P. Euzen and H. Toulhoat, *J. Catal.*, 2002, **211**, 1-5.
32. G. Paglia, C. E. Buckley, A. L. Rohl, B. A. Hunter, R. D. Hart, J. V. Hanna and L. T. Byrne, *Phys. Rev. B*, 2003, **68**, 144110.
33. M. Digne, P. Sautet, P. Raybaud, P. Euzen and H. Toulhoat, *J. Catal.*, 2004, **226**, 54-68.
34. E. Menéndez-Proupin and G. Gutiérrez, *Phys. Rev. B*, 2005, **72**, 035116.
35. G. Paglia, E. S. Božin and S. J. L. Billinge, *Chem. Mater.*, 2006, **18**, 3242-3248.
36. G. Paglia, C. E. Buckley and A. L. Rohl, *J. Phys. Chem. B*, 2006, **110**, 20721-20723.
37. M. Digne, P. Sautet, P. Raybaud, B. Rebours and H. Toulhoat, *J. Phys. Chem. B*, 2006, **110**, 20719-20720.
38. Y. G. Wang, P. M. Bronsveld, J. T. M. DeHosson, B. Djuricic, D. McGarry and S. Pickering, *J. Am. Ceram. Soc.*, 1998, **81**, 1655-1660.
39. G. Gutiérrez, A. Taga and B. Johansson, *Phys. Rev. B*, 2001, **65**, 012101.
40. R. Ahuja, J. M. Osorio-Guillen, J. Souza de Almeida, B. Holm, W. Y. Ching and B. Johansson, *J. Phys.: Condens. Matter*, 2004, **16**, 2891-2900.
41. H. P. Pinto, R. M. Nieminen and S. D. Elliott, *Phys. Rev. B*, 2004, **70**, 125402.
42. L. Jelver, P. M. Larsen, D. Stradi, K. Stokbro and K. W. Jacobsen, *Phys. Rev. B*, 2017, **96**, 085306.
43. Atomistix ToolKit version 2016.4, QuantumWise A/S (www.quantumwise.com)
44. M. Brandbyge, J. L. Mozos, P. Ordejón, J. Taylor and K. Stokbro, *Phys. Rev. B*, 2002, **65**, 165401.
45. T. Markussen, A. P. Jauho and M. Brandbyge, *Phys. Rev. B*, 2009, **79**, 035415.
46. M. Büttiker, Y. Imry, R. Landauer and S. Pinhas, *Phys. Rev. B*, 1985, **31**, 6207-6215.

47. K. Esfarjani, M. Zebarjadi and Y. Kawazoe, *Phys. Rev. B*, 2006, **73**, 085406.
48. H. Karamitaheri, M. Pourfath, H. Kosina and N. Neophytou, *Phys. Rev. B*, 2015, **91**, 165410.
49. G. M. Psofogiannakis, J. F. McCleerey, E. Jaramillo and A. C. T. Van Duin, *J. Phys. Chem. C*, 2015, **119**, 6678-6686.
50. A. C. T. Van Duin, S. Dasgupta, F. Lorant and W. A. Goddard, *J. Phys. Chem. A*, 2001, **105**, 9396–9409.
51. D. Gall, *J. Appl. Phys.*, 2016, **119**, 085101.
52. C. J. Powell and A. Jablonski, *Surf. Interface Anal.*, 2000, **29**, 108–114.
53. G. Zhang, Nanoscale Energy Transport and Harvesting: A Computational Study, Pan Stanford Publishing, 2014.
54. M. G. Muraleedharan, A. Rohskopf, V. Yang and A. Henry, *AIP Adv.*, 2017, **7**, 125022.
55. K. Hirose, K. Kobayashi, M. Shimono, H. Ishii and N. Kobayashi, *e-J. Surf. Sci. Nanotech.*, 2014, **12**, 115-118.
56. R. H. French, D. J. Jones and S. Loughin, *J. Am. Ceram. Soc.*, 1994, **77**, 412-422.

Figure Captions

Figure 1. Schematic representation of two-probe device model with channel region of metal-ceramic interface constructed between (100) surfaces of γ-Al_2O_3 and Al.

Figure 2. (a) 1D projection of average EDP curve against the fractional C-coordinate of the device as referred in figure 1; (b) Cut-plane image for EDP showing ΔV_E along the (B, C) plane across the interface; and (c) Contour plot showing the spatial distribution of EDD across the interface.

Figure 3. Energy-position resolved LDOS diagram for the interface along with 1D projection of electron transmission curve. The abscissa in LDOS diagram indicates the Cartesian coordinate of the central region along the C-direction of the device; and the color bar denotes the DOS amplitude. The energy on the Y-axis is relative to the Fermi energy of the interface.

Figure 4. Spin-resolved PDDOS spectra obtained from the analyses of DOS projected onto the atomic sites of the device: (a) close to the interface, and (b) close to the Al_2O_3 electrode.

Figure 5. Transmission spectrum of the Al/γ-Al_2O_3 interface at zero bias.

Figure 6. Plot of phonon thermal conductance as a function of temperature.

Figure 7. Variations of (a) thermoelectric figure of merit and (b) Seebeck coefficient with Fermi level position at different temperatures.

Figure 8. The temperature dependence of (a) electrical conductance, (b) Seebeck coefficient, (c) power factor, (d) electrical and phonon thermal conductance, (e) total thermal conductance, and (f) thermoelectric figure of merit.

Figure 9. Current-voltage characteristic curve of two-probe device of Al/γ-Al_2O_3 interface.

Figure 10. Computed energy-position resolved LDOS diagrams along with 1D projection of electron transmission curves under forward bias ($V_b > 0\ V$) and reverse bias ($V_b < 0\ V$) conditions: (a) + 0.7 V and (b) – 0.7 V.

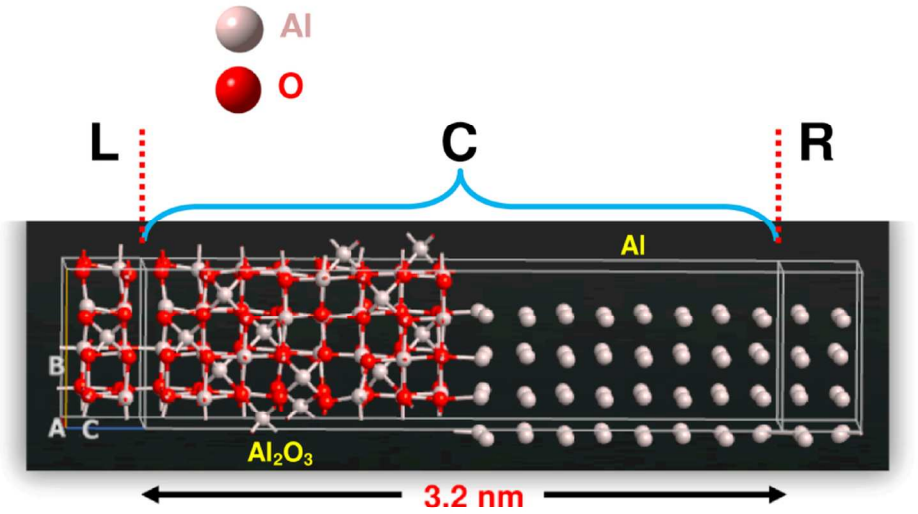

Figure 1

Figure 1. Schematic representation of two-probe device model with channel region of metal-ceramic interface constructed between (100) surfaces of γ-Al2O3 and Al.

Figure 1. Schematic representation of two-probe device model with channel region of metal-ceramic interface constructed between (100) surfaces of γ-Al2O3 and Al.

Figure 1. Schematic representation of two-probe device model with channel region of metal-ceramic interface constructed between (100) surfaces of γ-Al2O3 and Al.

110x95mm (300 x 300 DPI)

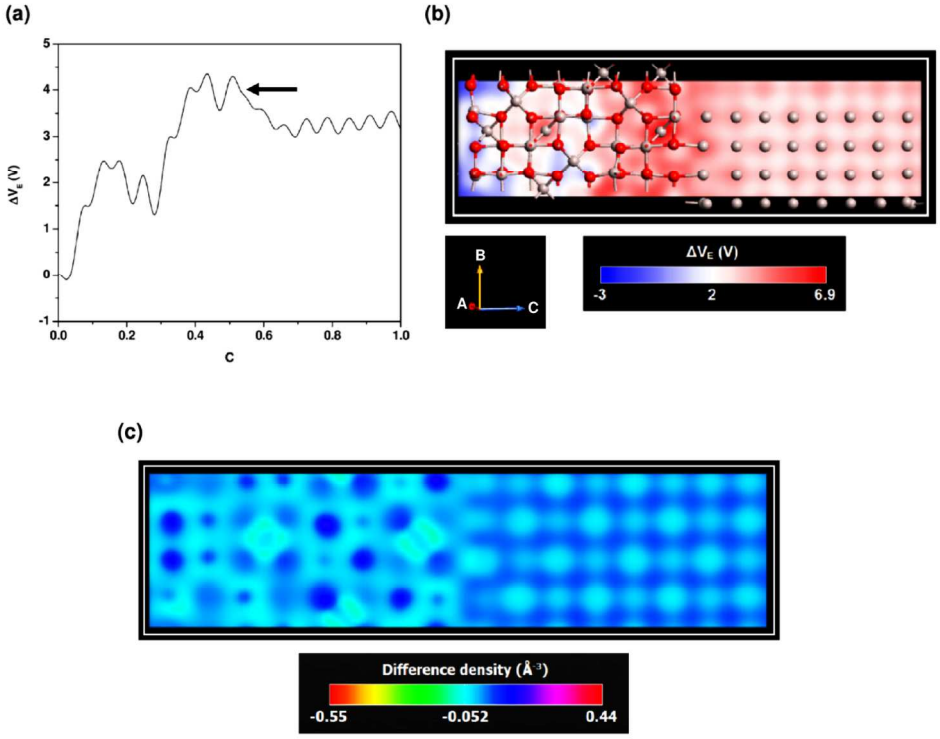

Figure 2

Figure 2. (a) 1D projection of average EDP curve against the fractional C-coordinate of the device as referred in figure 1; (b) Cut-plane image for EDP showing ΔV_E along the (B, C) plane across the interface; and (c) Contour plot showing the spatial distribution of EDD across the interface.

180x168mm (300 x 300 DPI)

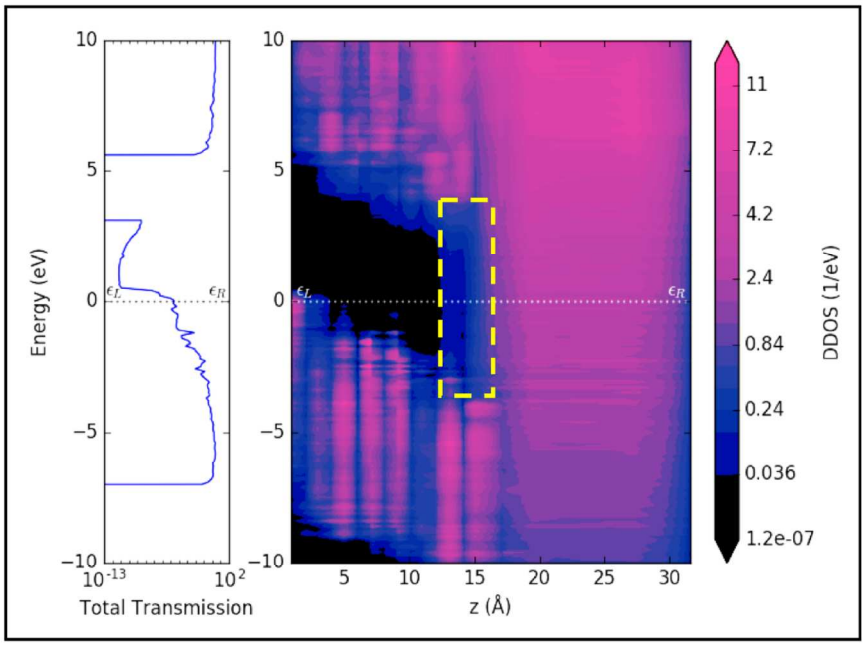

Figure 3

Figure 3. Energy-position resolved LDOS diagram for the interface along with 1D projection of electron transmission curve. The abscissa in LDOS diagram indicates the Cartesian coordinate of the central region along the C-direction of the device; and the color bar denotes the DOS amplitude. The energy on the Y-axis is relative to the Fermi energy of the interface.

156x145mm (300 x 300 DPI)

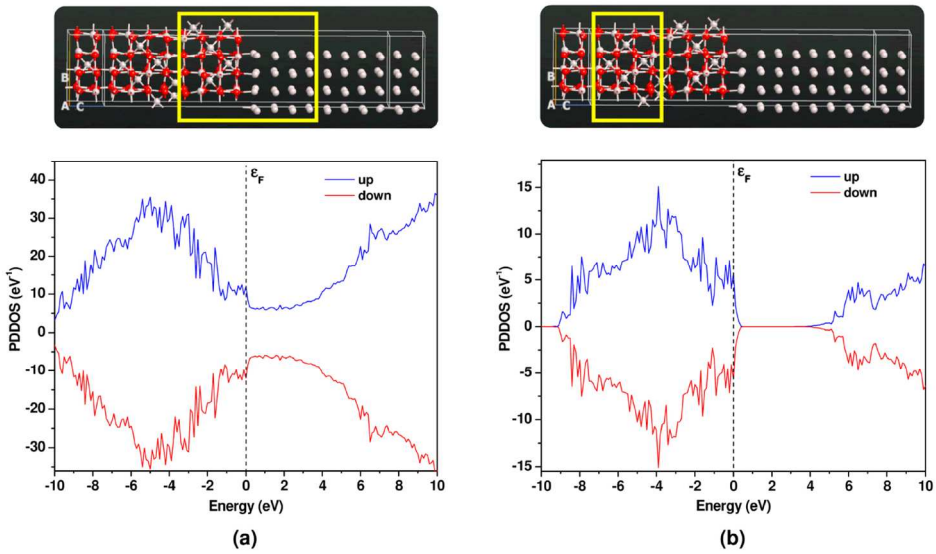

Figure 4

Figure 4. Spin-resolved PDDOS spectra obtained from the analyses of DOS projected onto the atomic sites of the device: (a) close to the interface, and (b) close to the Al2O3 electrode.

142x103mm (300 x 300 DPI)

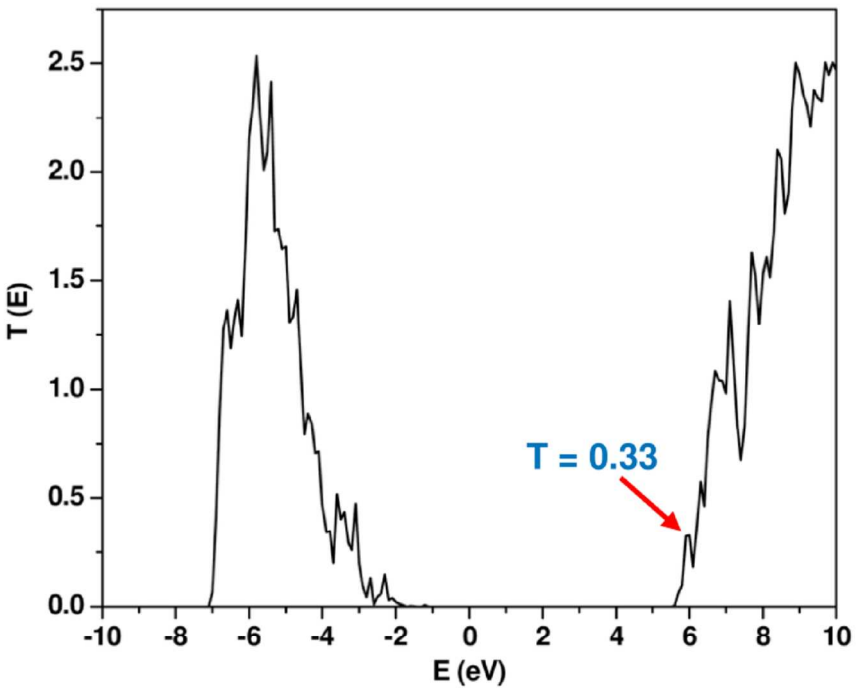

Figure 5

Figure 5. Transmission spectrum of the Al/γ-Al2O3 interface at zero bias.

110x114mm (300 x 300 DPI)

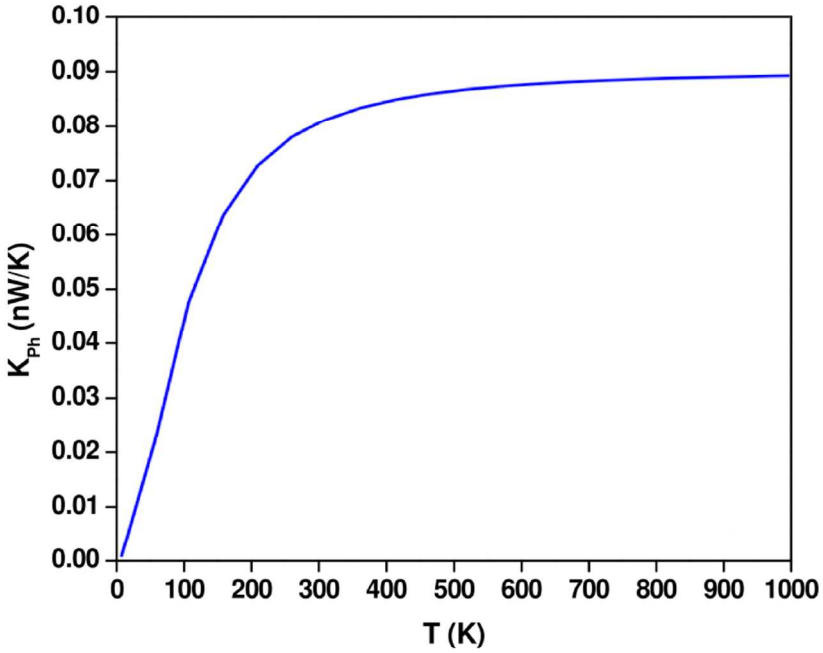

Figure 6

Figure 6. Plot of phonon thermal conductance as a function of temperature

120x114mm (300 x 300 DPI)

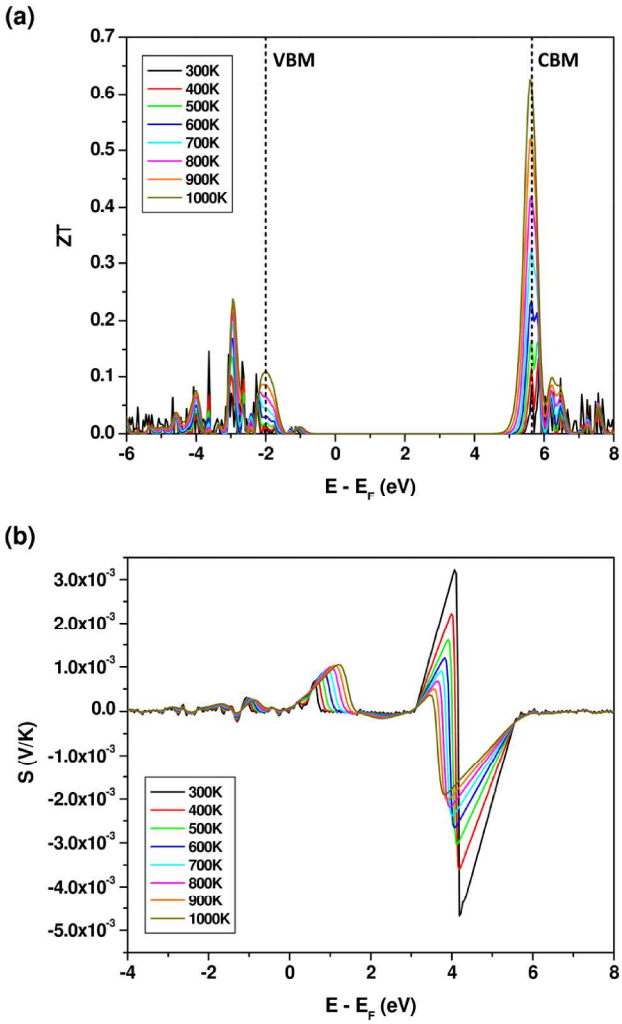

Figure 7

Figure 7. Variations of (a) thermoelectric figure of merit and (b) Seebeck coefficient with Fermi level position at different temperatures.

220x353mm (300 x 300 DPI)

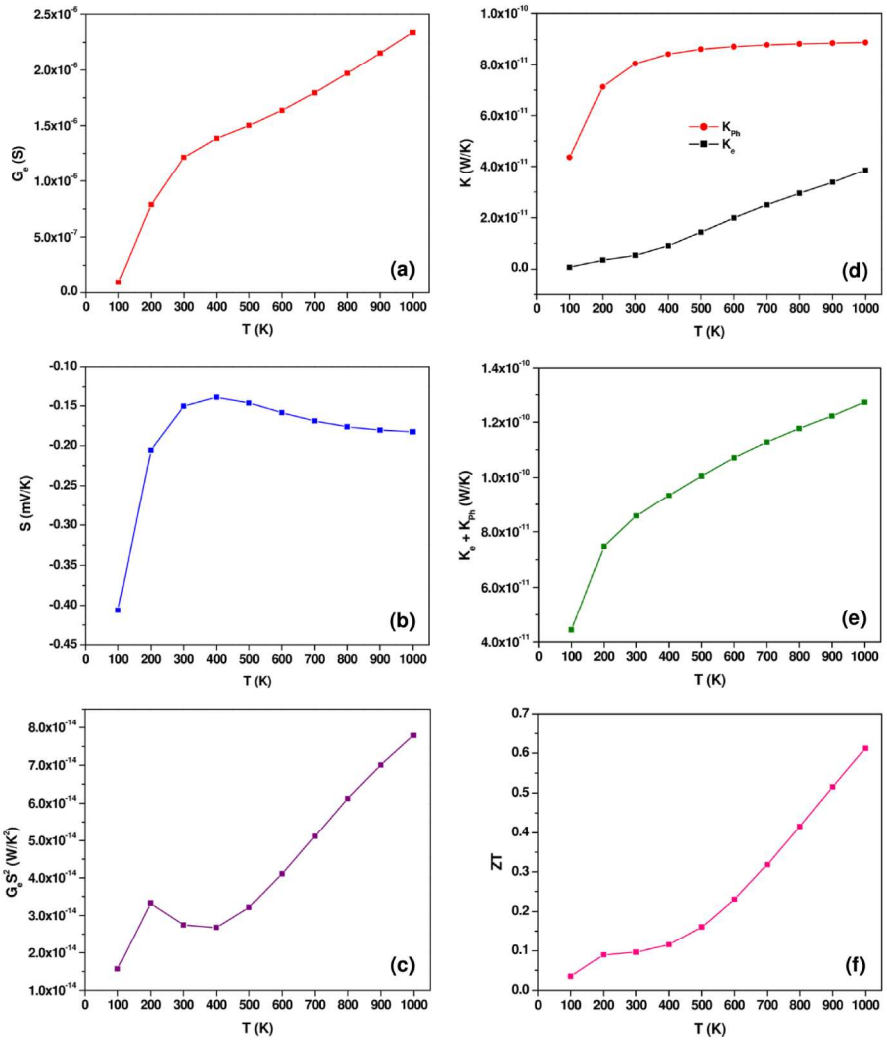

Figure 8

Figure 8. The temperature dependence of (a) electrical conductance, (b) Seebeck coefficient, (c) power factor, (d) electrical and phonon thermal conductance, (e) total thermal conductance, and (f) thermoelectric figure of merit.

Figure 8. The temperature dependence of (a) electrical conductance, (b) Seebeck coefficient, (c) power factor, (d) electrical and phonon thermal conductance, (e) total thermal conductance, and (f) thermoelectric figure of merit.

Figure 8. The temperature dependence of (a) electrical conductance, (b) Seebeck coefficient, (c) power factor, (d) electrical and phonon thermal conductance, (e) total thermal conductance, and (f) thermoelectric figure of merit.

245x300mm (300 x 300 DPI)

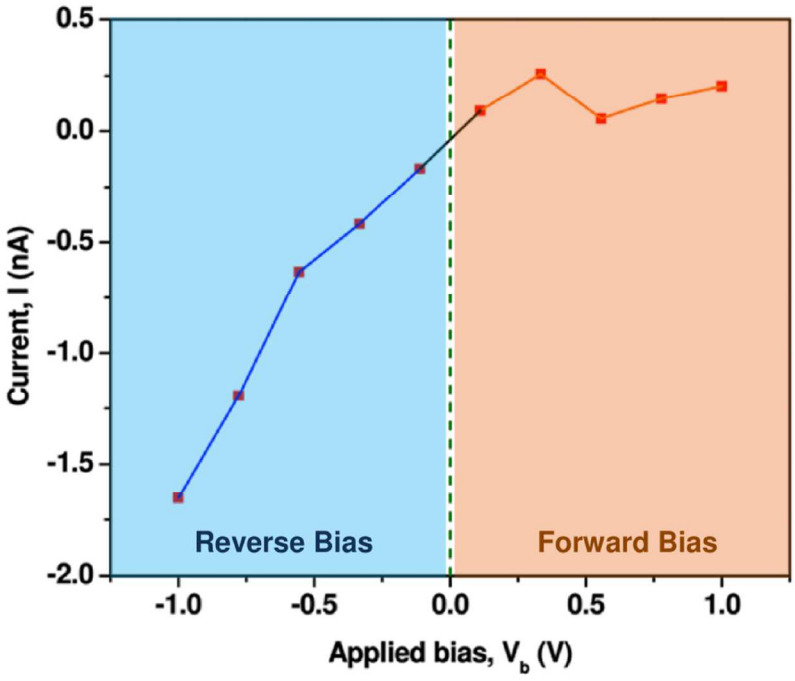

Figure 9

Figure 9. Current-voltage characteristic curve of two-probe device of Al/γ-Al2O3 interface.

130x128mm (300 x 300 DPI)

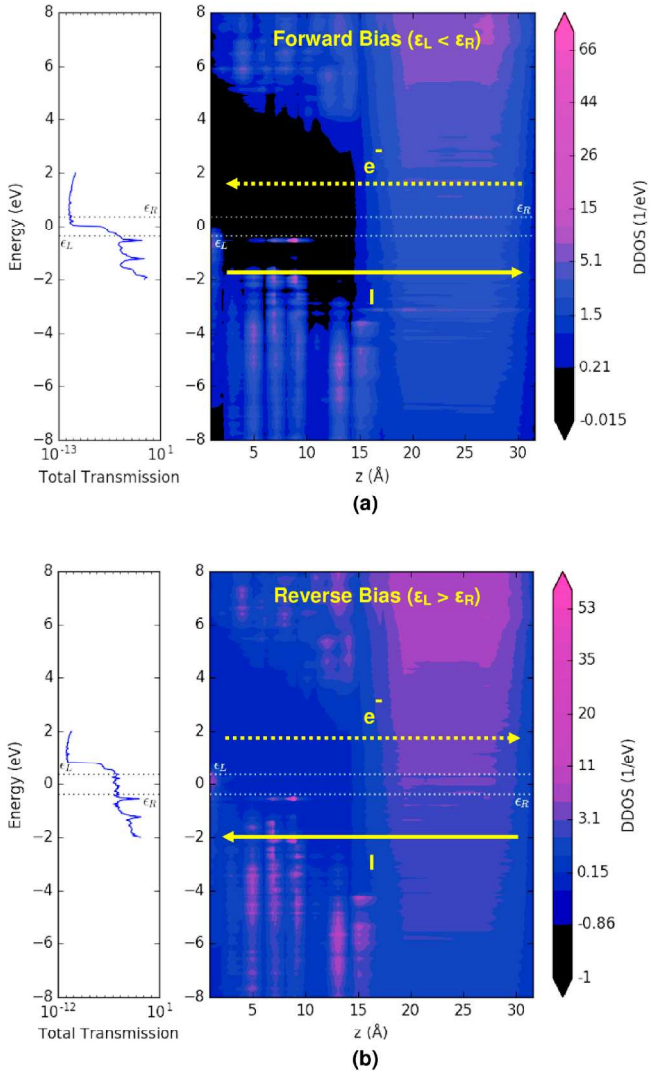

Figure 10

Figure 10. Computed energy-position resolved LDOS diagrams along with 1D projection of electron transmission curves under forward bias 〖(V〗_b >0 V) and reverse bias 〖(V〗_b <0 V) conditions: (a) + 0.7 V and (b) − 0.7 V.

247x394mm (300 x 300 DPI)